Received: 29 February 2024 | Revised: 24 June 2025 | Accepted: 9 July 2025

DOI: 10.1002/esp.70132

RESEARCH ARTICLE

ESPL WILEY

On the role of inherited rock fabric in critical zone porosity development: Insights from seismic anisotropy measurements using surface waves

Benjamin J. Eppinger[1] | W. Steven Holbrook[1] | Brady A. Flinchum[2,3] | Dario Grana[4] | Daniel de B. Richter[5] | Jorden L. Hayes[6] | Clifford S. Riebe[4] | Ciaran J. Harman[7,8] | Bradley J. Carr[4]

[1]Department of Geosciences, Virginia Polytechnic Institute and State University, Blacksburg, VA, USA

[2]School of Environmental and Life Sciences, University of Newcastle, Callaghan, Australia

[3]Previously at Department of Environmental Engineering and Earth Sciences, Clemson University, Clemson, SC, USA

[4]Department of Geology and Geophysics, School of Energy Resources, University of Wyoming, Laramie, WY, USA

[5]Nicholas School of the Environment, Duke University, Durham, North Carolina, USA

[6]Department of Earth Sciences, Dickinson College, Carlisle, PA, USA

[7]Department of Environmental Health and Engineering, Johns Hopkins University, Baltimore, MD, USA

[8]Department of Earth and Planetary Science, Johns Hopkins University, Baltimore, MD, USA

Correspondence
Benjamin J. Eppinger, Department of Geosciences, Virginia Polytechnic Institute and State University, Blacksburg, VA, USA.
Email: beppinger@vt.edu

Funding information
national science foundation GRFP; National Science Foundation, Grant/Award Numbers: 2012353, 2012227, 2012357, 2012316, 2012264

Abstract

Within Earth's critical zone, weathering processes influence landscape evolution and hillslope hydrology by creating porosity in bedrock, transforming it into saprolite and eventually soil. In situ weathering processes drive much of this transformation while preserving the rock fabric of the parent material. Inherited rock fabric in regolith makes the critical zone anisotropic, affecting its mechanical and hydrological properties. Therefore, quantifying and studying anisotropy is an important part of characterising the critical zone, yet doing so remains challenging. Seismic methods can be used to detect rock fabric and infer mechanical and hydrologic conductivity anisotropy across landscapes. We present a novel way of measuring seismic anisotropy in the critical zone using Rayleigh and Love surface waves. This method leverages multi-component surface seismic data to create a high-resolution model of seismic anisotropy, which we compare with a nuclear magnetic resonance log measured in a nearby borehole. The two geophysical data sets show that seismic anisotropy and porosity develop at similar depths in weathered bedrock and both reach their maximum values in saprolite, implying that in situ weathering enhances anisotropy while concurrently generating porosity in the critical zone. We bolster our findings with in situ measurements of seismic and hydrologic conductivity anisotropy made in a 3 m deep soil excavation. Our study offers a fresh perspective on the importance of rock fabric in the development and function of the critical zone and sheds new insights into how weathering processes operate.

KEYWORDS
anisotropy, geophysics, hydrology, porosity, weathering

1 | INTRODUCTION

Within Earth's Critical Zone (CZ), near-surface weathering processes shape landscapes and influence hillslope hydrology by creating porosity in rock, breaking it down into saprolite and eventually soil (Brantley et al., 2007; Riebe et al., 2017). Weathering creates porosity in a variety of ways, such as chemical weathering, volumetric strain, fracturing/subcritical cracking and biological activity (Brantley, Eissenstat, et al., 2017; Brantley, Lebedeva, et al., 2017; Eppes & Keanini, 2017; J. L. Hayes et al., 2019; Lebedeva & Brantley, 2013; Molnar, 2004; Moon et al., 2017; Navarre-Sitchler et al., 2015; Pedrazas et al., 2021; Sak et al., 2010; Slim et al., 2015). To map the properties associated with these various processes, non-invasive geophysical methods are often used (Binley et al., 2015; Parsekian et al., 2015), of which, seismic methods have become increasingly popular due to the strong correlation between seismic wave speed

and porosity (Befus et al., 2011; Gardner et al., 1974; Holbrook et al., 2014; Hudson Rasmussen et al., 2023; Moravec et al., 2020; Trichandi et al., 2022; West et al., 2019). In several recent studies, velocity tomograms have been combined with geochemical data, remote sensing observations and numerical models to link the occurrence of porosity in the CZ with weathering processes (Callahan et al., 2020, 2022; J. L. Hayes et al., 2019; Holbrook et al., 2019; Ma et al., 2021; Moravec et al., 2020; Seyfried et al., 2018; St. Clair et al., 2015; West et al., 2019).

While many studies have used geophysical methods to infer spatial variations in bulk porosity throughout the CZ, it remains relatively difficult to relate geophysical observations with the structure of porosity. Nonetheless, constraining these characteristics is important because a material's pore alignment and orientation may determine if and how it is mechanically or hydrologically anisotropic. CZ materials inherit their properties from the underlying protolith (Rich, 1956), which often show some type of mechanical or hydrological anisotropy to begin with. Moreover, mechanical and hydrological anisotropy in the CZ have major implications for landscape evolution and function. Several past studies have demonstrated that regolith may possess hydrologic conductivity anisotropy (Mirus, 2015; Zaslavsky & Rogowski, 1969), influencing the flow and infiltration of water and subsequently regulating the extent of chemical weathering across landscapes (Leone et al., 2020; Novitsky et al., 2018; Pradhan et al., 2022). Studies on landslide hazards have shown that mass-wasting events may be more prevalent in areas underlain by foliated or bedded rocks (Roth, 1983). Due to the mechanical anisotropy of CZ materials in such areas, failure is more likely to occur along planes coincident with rock fabric (Glastonbury & Fell, 2010). Thus, inherited rock fabric in the CZ can significantly affect the function of landscapes. Despite influencing CZ processes in fundamental ways, mechanical and hydrological anisotropy are difficult to study and characterise over large areas.

While the most straightforward way to constrain mechanical or hydrological anisotropy is to use direct measurements from the field and/or lab (Acosta & Violay, 2020; Clavaud et al., 2008; Walsh & Brace, 1964), it is challenging to collect enough data in this manner to characterise the CZ at the landscape scale. Measuring seismic anisotropy offers one way to indirectly infer hydrological and mechanical anisotropy over large spatial extents. Past studies have shown that seismic anisotropy caused by inherited rock fabric can be quantified and mapped across landscapes (e.g., Novitsky et al., 2018).

In this work, we present a new method of delineating anisotropy in the CZ using surface waves. We use this method to construct a 2D pseudo-tomogram mapping the spatial degree and extent of anisotropy in regolith. We also present the first comparison of seismic anisotropy measurements and nuclear magnetic resonance (NMR) derived porosity data in weathered materials. We show that the two correlate strongly, implying that weathering creates seismic anisotropy and porosity concurrently. We integrate these findings with in-situ measurements of seismic and hydrologic conductivity anisotropy made in a 3-m-deep soil excavation. By synthesising these results with existing literature on weathering processes, we seek to improve our conceptual understanding of how porosity is generated in the CZ. Before introducing our data and results, we provide the reader with a primer on elastic wave propagation and how various data collection strategies can be leveraged to elucidate seismic anisotropy in the CZ.

2 | SEISMIC WAVE PROPAGATION IN THE CRITICAL ZONE

Seismic methods have long been employed to investigate Earth's structure on regional and global scales (Fichtner et al., 2024; Tromp, 2019), and more recently, these methods have gained prominence in the study of the critical zone (Holbrook et al., 2014; Singha et al., 2024). Seismic waves include both body waves (P and S – waves) and surface waves (Rayleigh and Love waves). Most seismic studies of the CZ to date have used P-waves to constrain CZ structure. However, a few studies have also used S-waves (e.g., Flinchum et al., 2024) or Rayleigh surface waves (e.g., Trichandi et al., 2022) to constrain shear wave velocity (Vs) as well. Here we present results from both Rayleigh and Love surface waves to constrain seismic anisotropy.

Seismic wave propagation in anisotropic media exhibits complex behaviour, in part due to directional variations in wave speed. Seismologists can exploit this phenomenon by deploying geophone arrays and recording waveforms at Earth's surface to gauge the presence of dipping fabrics such as fractures and foliation (Okaya et al., 2019; Okaya & Christensen, 2002; Okaya & McEvilly, 2003). For example, by using circular arrays of geophones, seismic anisotropy has been studied in the CZ to quantify the prevalence of dipping inherited rock fabric. Novitsky et al. (2018) were the first to use circular arrays of geophones to map variations in seismic anisotropy across landscapes, while Eppinger et al. (2021) modified the circular array method to better quantify variations in seismic anisotropy with depth. While both Novitsky et al. (2018) and Eppinger et al. (2021) used P-waves to quantify seismic anisotropy, to our knowledge, surface waves have not previously been used to measure seismic anisotropy in the CZ.

While also exhibiting directional variations in wave speed, surface waves in anisotropic media may propagate at different velocities depending on their polarization (e.g., Okaya et al., 2019; Okaya & Christensen, 2002; Okaya & McEvilly, 2003). This characteristic can exasperate differences between Rayleigh and Love waves, as Rayleigh waves are polarized in the vertical plane and Love waves are polarized in the horizontal (Endrun et al., 2008; Huang et al., 2010; Raykova & Nikolova, 2003; Xie et al., 2013). When the underlying rock fabric is parallel with Earth's surface, the anisotropy observed in Rayleigh and Love waves is termed radial anisotropy, and can be measured using multi-component geophones (Duret et al., 2010; Friederich & Huang, 1996; Montagner & Nataf, 1986; Raykova & Nikolova, 2003). In numerous continental-scale seismology studies, radial anisotropy has been quantified using surface waves (Endrun et al., 2008; Huang et al., 2010; Raykova & Nikolova, 2003; Xie et al., 2013); however, to our knowledge, ours is the first study to adapt these methods for the CZ.

3 | STUDY SITE BACKGROUND

The South Carolina Piedmont site (SCP) is located in the Appalachian Piedmont physiographic province, about 15 km southwest of Union, SC (Figure 1). From approximately 1750 to 1957, the area was intensively farmed to produce commercial crops such as cotton (Richter et al., 2014). These farming practices accelerated soil erosion rates at SCP, but since 1957, reforestation has stabilised the landscape

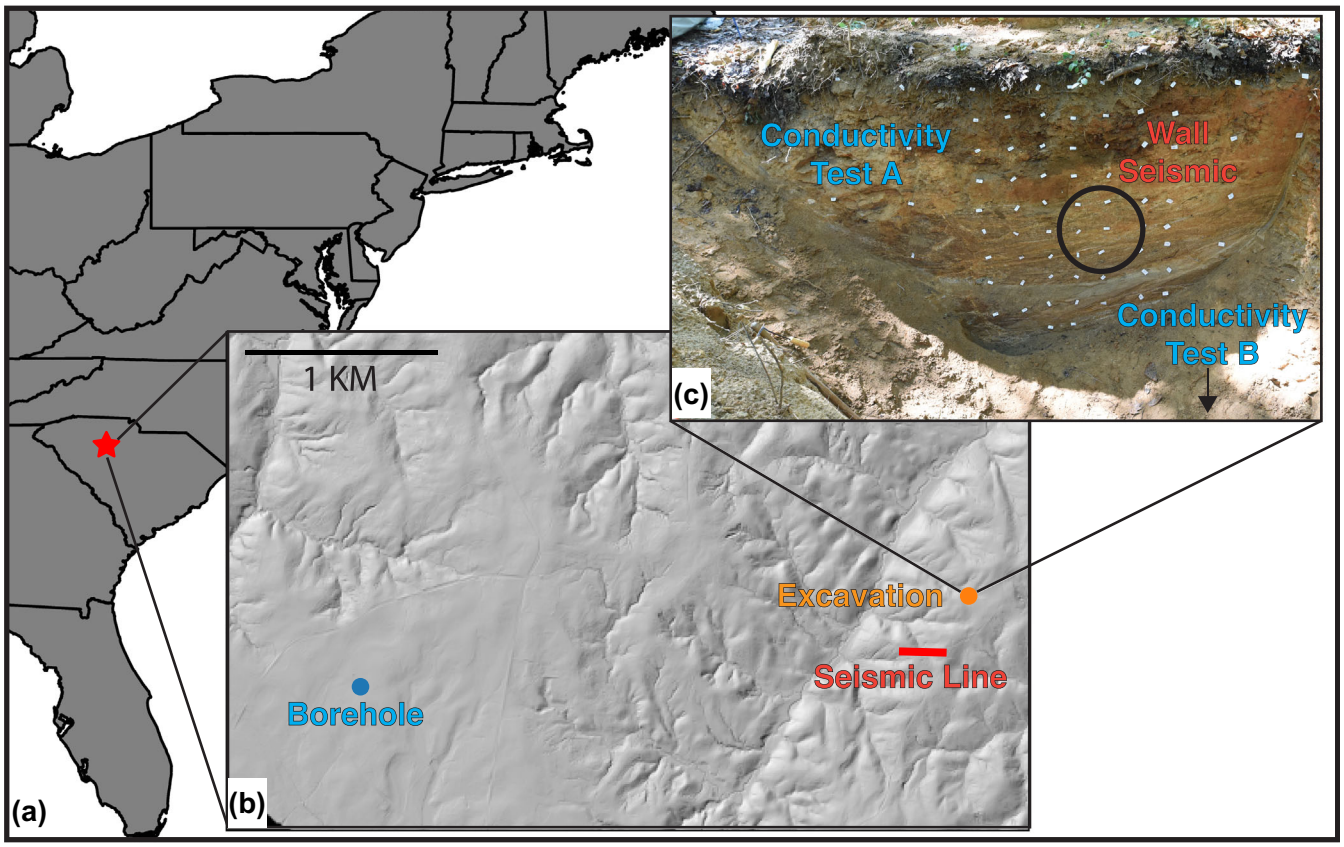

FIGURE 1 Panel a shows a map of the eastern United States with the South Carolina Piedmont site marked by a red star. Inset panel B shows a hill shade map of the SCP area with a blue dot demarcating the location of the borehole logged by Holbrook et al. (2019). The red line in panel B demarcates the location of the seismic profile, and the orange dot shows the location of the soil excavation. Inset panel C contains a photograph of a wall of the soil excavation. In panel C, the approximate locations of the circular seismic array and one of the constant head infiltration tests are labelled. The second constant head infiltration test was located on the opposite wall of the excavation as indicated by the arrow next to the label.

morphology (Bonetti et al., 2019). The growth of pine forests in the past decades has also sequestered significant amounts of carbon and altered the soil chemistry (Richter et al., 1999; Richter et al., 2014). These changes have been well documented by soil sampling at the site since 1962 (Richter et al., 1999). The topography of SCP is characterised by moderate to steep hillslopes connecting interfluves and valleys with relief of 10s of meters (Figure 1b). The area is subject to a humid, subtropical climate and subsequently, thick Ultisols tend to mantle the landscape (Richter et al., 2014).

At a farm adjacent to SCP, Holbrook et al. (2019) drilled and logged a borehole with nuclear magnetic resonance (NMR), which produced a vertical water content profile. We utilise this previously published NMR data later in subsection 4.5. The drilling effort by Holbrook et al. (2019) showed the underlying bedrock to be a granitic gneiss bearing a mineralogical composition of roughly 38% plagioclase, 28% quartz, 22% orthoclase, 4% biotite and 3% epidote. In the summer of 2021, we collected more data at SCP, including a profile of multi-component seismic data as well as in situ measurements of mechanical and hydrological anisotropy from a 3 m deep soil excavation. These in situ measurements were collected using a small circular array of geophones placed on the excavation wall and constant head infiltration tests at two locations within the excavation. In the following sections, we provide more details on the data collection and processing methods, as well as the subsequent results.

4 | METHODS AND RESULTS

In this study, we integrate multiple methods and data sets to investigate various types of anisotropy in the CZ. By analysing surface waves, we constrain radial anisotropy over a large spatial area. We also present in situ measurements of mechanical and hydrologic conductivity anisotropy taken on the wall of a ~ 3 m deep soil excavation (Figure 1c). We synthesise our data with a previously published NMR log (Holbrook et al., 2019) to garner further insights into CZ processes and anisotropy. Because we use several data sets in this study, immediately after detailing each data collection method, we discuss the corresponding results. In the discussion section, we go on to integrate the results from all the methods together and contextualize our findings with respect to existing literature on weathering processes.

4.1 | Radial anisotropy measurements from two-component surface seismic data

Surface wave dispersion measurements have long been used to infer Earth's structure, relying on the fact that lower-frequency energy penetrates deeper into the subsurface while higher-frequency energy is more sensitive to shallower material (Haskell, 1951). Therefore, vertical variations in the Earth's structure cause different frequencies of seismic energy to travel at different speeds, a phenomenon known as

phase velocity dispersion (Park et al., 1998). Seismologists have created forward models that can predict the phase velocity response of a given one-dimensional earth model, as well as inversion algorithms that use the forward model to estimate the earth's velocity structure by fitting dispersion curve information (Xia et al., 1999). In this work, we use the popular Computer Programs in Seismology software package which employs a weighted least squares algorithm to invert both Rayleigh and Love wave dispersion curves (Herrmann, 2013).

The ability to invert data from both Rayleigh and Love waves is nontrivial because the two wave types exhibit different depth sensitivities (Herrmann & Ammon, 2007; Raykova & Nikolova, 2003). Hence, even in an isotropic setting, it is common for Rayleigh wave dispersion measurements to appear slower than Love wave dispersion measurements (Friederich & Huang, 1996). This necessitates the use of dispersion inversion to constrain anisotropy as opposed to merely comparing Rayleigh and Love wave dispersion curves (Raykova & Nikolova, 2003). For example, in the isotropic case, Herrmann's (2013) inversion algorithm can constrain identical velocity-depth profiles from differing Rayleigh and Love wave dispersion curves. Alternatively, in anisotropic settings, Rayleigh and Love waves differ in velocity sensitivity, with Rayleigh Waves being sensitive to the seismic velocity of vertically polarized energy, Vs_v and Love waves being sensitive to the seismic velocity of horizontally polarized energy, Vs_h (Friederich & Huang, 1996). Therefore, Rayleigh and Love wave dispersion curves can be inverted separately to obtain independent estimates of Vs_v and Vs_h, which can subsequently be used to quantify anisotropy (Endrun et al., 2008; Huang et al., 2010). For instance, Raykova & Nikolova (2003) constrained radial anisotropy by using the Computer Programs in Seismology software package to independently invert Rayleigh and Love wave dispersion curves, and in this work, we employ a similar strategy.

In the following subsections, we detail how we collected surface seismic data to generate high-resolution dispersion measurements. We also give a conceptual overview of our workflow for inverting dispersion curves, quantifying uncertainty and estimating anisotropy. The interested reader can find more information about our workflow in the supplementary information and can reference Herrmann (2013) as well as Herrmann & Ammon (2007) for more details of the surface wave dispersion inversion algorithm.

4.2 | Surface seismic data collection and processing

For near-surface velocity characterization, it is common practice to use linear arrays of geophones to collect seismic data, which usually results in data that can produce high-quality dispersion curve measurements (Socco & Strobbia, 2004). We collected surface seismic data using two collocated linear arrays of 96 geophones. One array consisted of instruments measuring vertical particle velocity, while the other array comprised instruments measuring particle velocity in the direction perpendicular to the trend of the profile. We used a constant geophone spacing of 2 m, which according to Nyquist-Shannon theorem, allows us to sample seismic wavelengths as small as 4 m. Both the horizontal and vertical component geophones have a flat frequency response from 4.5 Hz up to 1,000 Hz. Every 10 m along the profile, a sledgehammer was swung in three different directions: vertically, and horizontally in opposing cross-line orientations. The resultant wavefields were recorded with a sampling rate of 0.125 ms for 0.5 s after impact and have most of their energy concentrated between 10 and 110 Hz.

We processed these ground-motion data to construct and invert dispersion curves associated with Love and Rayleigh Waves. To enhance the spatial resolution of the surface wave inversion, we used data windowing methods (Bergamo et al., 2012; Pasquet & Bodet, 2017; Trichandi et al., 2022), which involved computing local dispersion curves for traces within a 30 m wide window using all the sources within 10 m of either side of the window. We then stacked all the dispersion curves for the vertical and horizontal components separately and manually picked phase velocities within the frequency range of 10–45 Hz (Figure 2). Thereafter, we inverted the picked dispersion curves to infer a one-dimensional shear wave velocity vs depth model using a combined deterministic and data assimilation approach. These steps were repeated for each data window, the first of which is centred at 20 m along the transect, the next at 30 m and so on until the last data window at 160 m.

4.3 | Dispersion curve inversion and uncertainty quantification

Although deterministic surface wave dispersion methods are widely used (Herrmann, 2013), a persistent challenge in using these algorithms is the dependency on the starting model and model nonuniqueness. A poorly chosen starting model can lead to inaccurate inversion results, and even if a model fits the data well, there may be other models that are just as good (Pasquet & Bodet, 2017; Socco et al., 2010; Socco & Strobbia, 2004; Xia et al., 1999). To mitigate these issues, ensemble approaches are often employed in studies using surface wave dispersion inversion (Duret et al., 2010; Raykova & Nikolova, 2003). These approaches generally involve performing multiple deterministic inversions of dispersion data using a set of initial models. The average of the inverted models serves as a maximum likelihood estimate of the true velocity structure, while the standard deviation provides an estimate of uncertainty.

In this study, we generate an ensemble of 50 starting velocity models, each characterized by different velocity-depth functions that, on average, increase with depth. All the models are parameterized with a maximum depth of 30 m, which we chose to be between a half and one of the maximum wavelength (~40 m) of the observed phase velocities (Socco & Strobbia, 2004). We use the Computer Programs in Seismology software package to invert the ensemble of initial models, resulting in two sets of fitted models. One set corresponds to Vs_v and is derived from fitting Rayleigh wave (vertical component) dispersion curves, while the other corresponds to Vs_h and is derived by fitting Love wave (horizontal component) dispersion curves. However, the deterministic inversion process can sometimes yield models that either poorly fit the observed dispersion data or exhibit velocity abnormalities. To address this, we apply the ensemble smoother data assimilation technique to the inverted models, which helps prevent suboptimal models from skewing the results (Emerick & Reynolds, 2013; Evensen, 2009). A detailed description of the ensemble approach is provided in the supplementary materials.

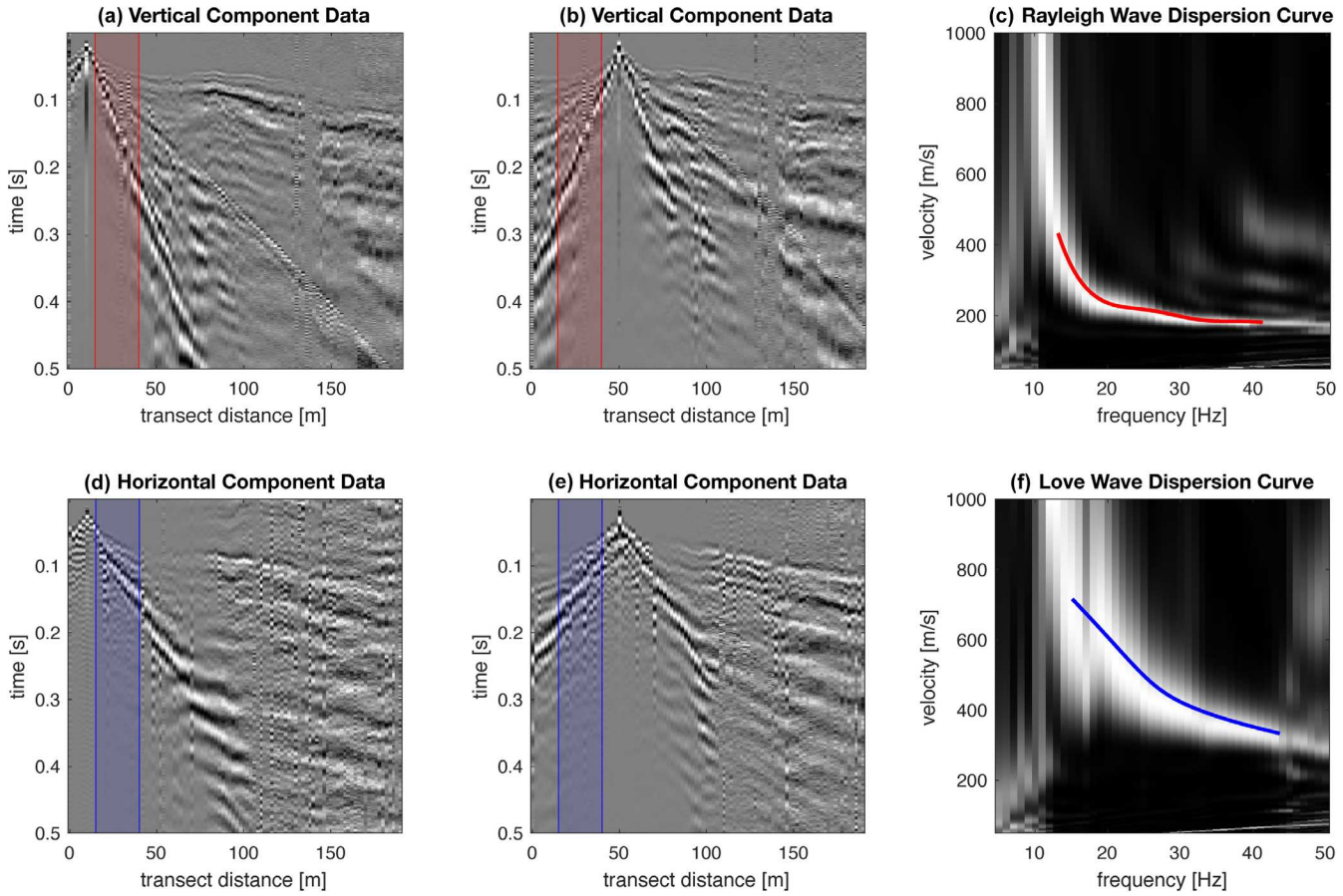

FIGURE 2 Panels A and B display seismic shot gathers collected using vertical instruments and sources. The red rectangles demarcate the data windows used to construct the dispersion image pictured in panel C. The red line in panel C shows the picked dispersion curve on the dispersion image. Panels D and E display seismic shot gathers collected using horizontal instruments and sources. The blue rectangles demarcate the data windows used to construct the dispersion image pictured in panel F. The blue line in panel F shows the picked dispersion curve on the dispersion image.

The procedure described above creates ensembles of one-dimensional velocity-depth functions at each data window, and we denote the average velocity-depth function from each ensemble as $\overline{Vs}(z)$ and the standard deviation depth function as $\sigma(z)$. To create a two-dimensional visualization of the results, we interpolate between ensembles at each data window to create pseudo tomograms of the Rayleigh and Love wave speed, $\overline{Vs_v}(x,z)$ and $\overline{Vs_h}(x,z)$ and their respective 2D standard deviation fields $\sigma_v(x,z)$ and $\sigma_h(x,z)$. Then we quantify the spatial uncertainty with respect to wave speed as $\sigma/\overline{Vs}$. Finally, we calculate per cent anisotropy measurements using the interpolated velocities and the following equation (Novitsky et al., 2018).

$$A(x,z) = \frac{\overline{Vs_h} - \overline{Vs_v}}{\frac{1}{2}\left(\overline{Vs_h} + \overline{Vs_v}\right)} * 100\% \quad (1)$$

4.4 | Surface wave imaging results

The one-dimensional inversion results at each data window show that the variance in the ensembles tends to grow with depth (e.g., Figure 3), which is expected considering that the data coverage decays with depth (Haskell, 1951; Pasquet & Bodet, 2017; Socco & Strobbia, 2004; Xia et al., 1999). Most of the inverted models fit the dispersion data well at higher frequencies, which may explain why the shallower parts of the models are better constrained. Conversely, the lower frequencies may not be fit as well by the inverted models, potentially explaining larger uncertainty bounds at depth. These trends are exemplified in Figure 3 and are also present in the inversions at other data windows. After interpolating between all the inversions, the same trends can be observed in panels c and d of Figure 4. Additionally, the Love wave dispersion inversion results tend to show greater uncertainty at depth than the Rayleigh wave results (Figure 4).

The velocity pseudosections displayed in panels a and b of Figure 4 show that the Love and Rayleigh velocities are notably different across the profile. At shallow depths, the Love wave speed may be significantly greater than the Rayleigh wave speed, while at greater depths, the Rayleigh and Love wave speeds tend to converge (Figures 3 and 4). This velocity structure leads to a persistent layer of intensely anisotropic material at depths of 1–15 m (Figure 5). These depths correspond with shear wave velocities between 300 and 700 m/s, which are indicative of saprolite (Flinchum et al., 2024; Trichandi et al., 2022). In the upper meter of the subsurface model, anisotropy measurements appear to decrease towards the surface.

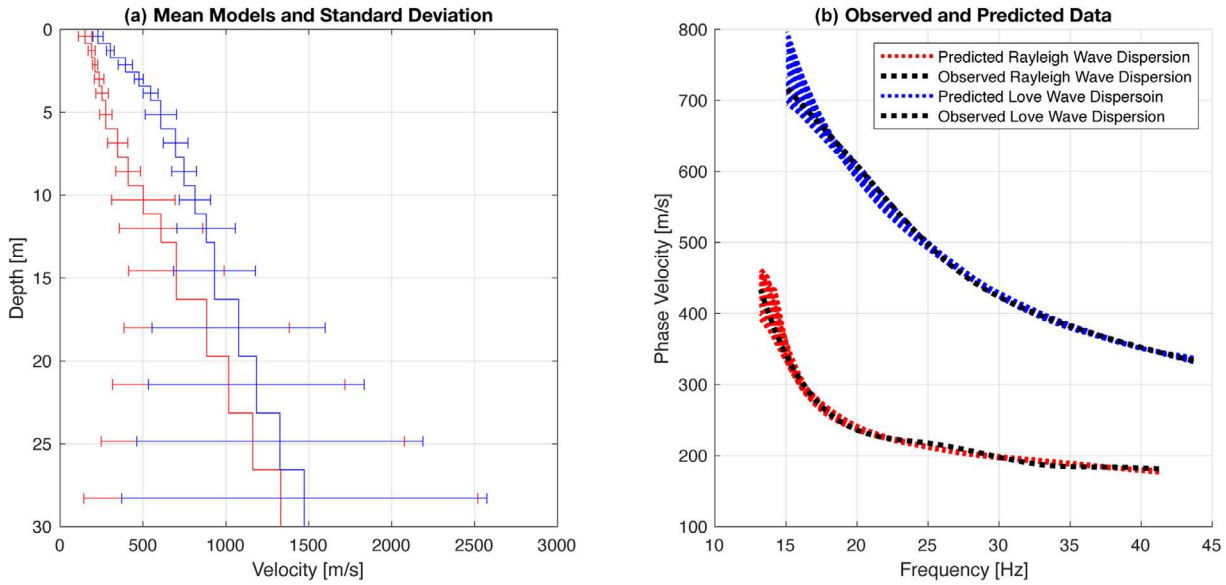

FIGURE 3 Panel a shows the one-dimensional inversion results after both the deterministic and data assimilation steps for the data window highlighted in Figure 2, which is centred at 30 m along the seismic transect. The red and blue lines show the mean velocity profiles derived for Rayleigh and love waves, respectively. The error bars show the standard deviation. The black lines in panel B show the picked dispersion curves for Rayleigh and love waves. The red and blue dots show predicted dispersion data for the deterministic Rayleigh and love wave models, respectively.

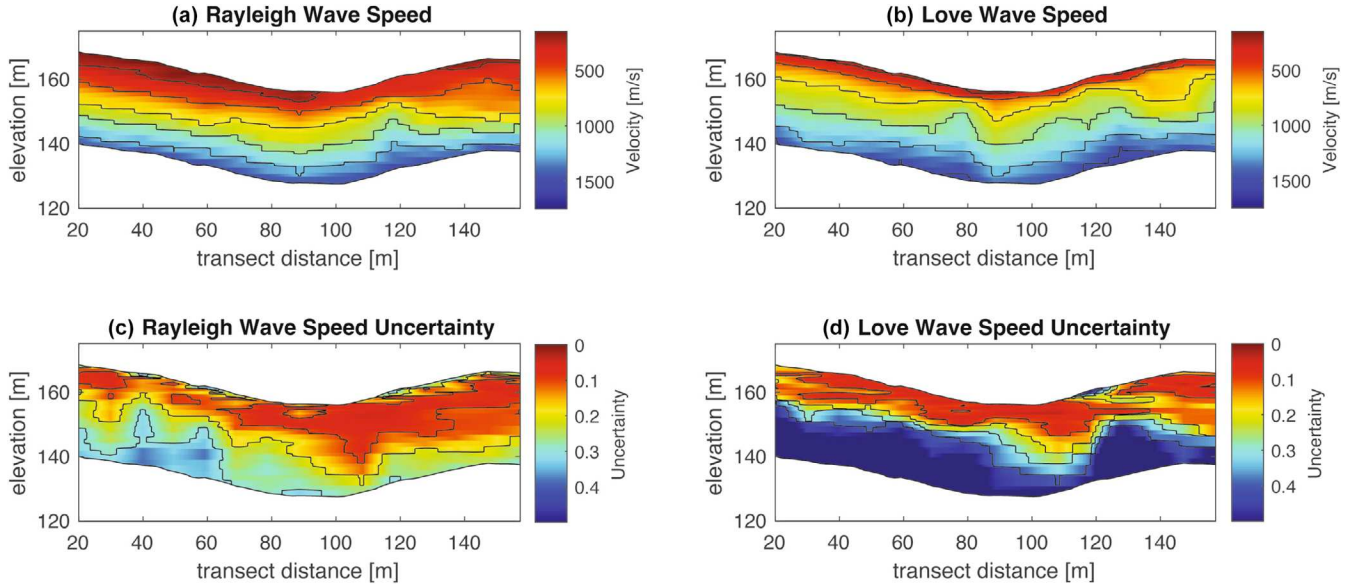

FIGURE 4 Results from surface seismic data collected along the transect shown in Figure 1B. Panel a shows the inverted and interpolated shear wave velocity field using Rayleigh waves. Panel B shows the inverted and interpolated shear wave velocity field using love waves. Panels C and D show the uncertainty fields for Rayleigh and love wave velocity respectively as defined in section 4.3. In panels A and B, the black lines are velocity contours spaced at increments of 250 m/s. in panels C and D, the black lines are uncertainty ($\sigma/\overline{Vs}$) contours spaced at increments of 0.1.

4.5 | Comparison between anisotropy measurements and NMR data

The surface wave anisotropy imaging provides a new picture of the CZ, which shows remarkable similarities with the previously published NMR log (Holbrook et al., 2019). Nuclear magnetic resonance operates by generating an electromagnetic field that polarizes molecules containing magnetic nuclei, such as hydrogen atoms in water. By measuring the response of these nuclei to the induced field, NMR can estimate the quantity of hydrogen atoms, which in turn provides an estimate of the water volume present. Therefore, when applied to saturated materials below the water table, NMR enables the estimation of porosity (Hertrich, 2008; Parsekian et al., 2015). Anisotropy measurements and NMR data are complementary, because while knowledge of anisotropy elucidates the preferential alignment of porosity, NMR data constrain total porosity. To compare how porosity and seismic anisotropy vary with depth, we first compute an average anisotropy profile from the surface seismic data. The term "average" refers to taking the mean of all the one-dimensional seismic anisotropy profiles created at each data window along the transect.

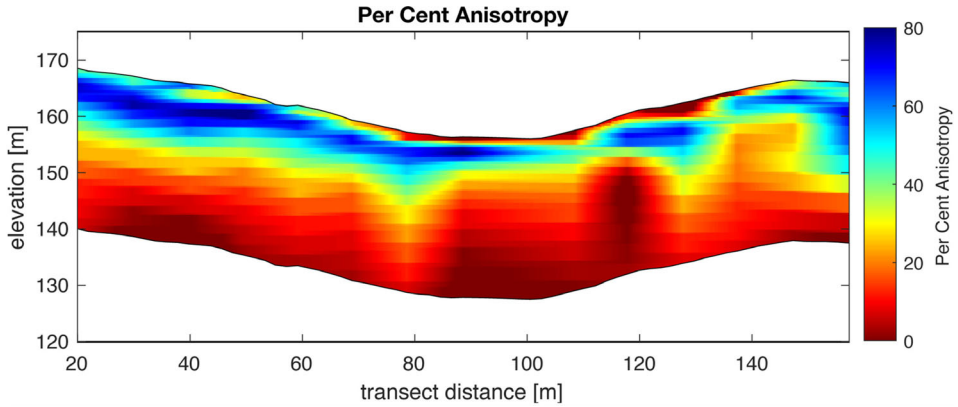

FIGURE 5 Per cent anisotropy pseudosection derived using panels A and B from Figure 4 and equation 1.

Figure 6 shows that seismic anisotropy and porosity begin to develop at 18 m depth, where Holbrook et al. (2019) delineate the boundary between saprolite and fractured bedrock. Above the fractured bedrock, where weathering processes are more active, both seismic anisotropy measurements and porosity increase rapidly (Figure 6). At depths of 3–8 m, which Holbrook et al. (2019) characterise as saprolite, seismic anisotropy measurements and porosity attain their maximum values of ~60%. In the very near surface, seismic anisotropy measurements decrease, particularly at depths where there may be soil. At these shallow depths, there are no conclusive NMR data because the material is above the water table and therefore unsaturated. Note that the seismic anisotropy profile and NMR log are not collocated but are within 3 km of each other. Therefore, Figure 6 is intended to present general trends in how porosity and seismic anisotropy vary with depth at SCP rather than collocated measurements of porosity and anisotropy.

Overall, Figure 6 suggests that porosity and seismic anisotropy are correlated in saturated weathered materials. In fact, further analysis shows that for measurements below the water table, the NMR porosity and average seismic anisotropy data have a Pearson correlation coefficient of 0.93. Additional regression analysis between the NMR porosity and seismic anisotropy variables demonstrates that the two exhibit a strong linear relationship with an R^2 value of 0.86 (Figure S3). These results should be taken with the caveat that the NMR porosity data and seismic anisotropy model have different depth resolutions. The NMR porosity data is sampled at evenly spaced depth intervals, while the seismic anisotropy models are parameterized by layers that increase in thickness with depth (Figures 3 and 6). Furthermore, uncertainty in the seismic anisotropy data increases significantly with depth (Figures 3 and 4) while the NMR porosity data is fairly accurate at all depths below the water table.

4.6 | In situ measurements from the soil excavation

While the surface seismic results provide spatially extensive measurements of anisotropy, in situ data, such as the NMR data shown above, provide critical context for the seismic results. To further refine our interpretation of radial anisotropy in the critical zone, we introduce in situ measurements of seismic and hydrological anisotropy, helping to demonstrate the relationship between the two. Both types of in situ measurements were collected in the 3 m deep soil excavation discussed in section 3. The soil excavation is situated on an interfluve at a relatively high elevation in the landscape. A backhoe was used to dig to refusal at the weathered bedrock horizon, which was encountered roughly 3 m below the ground surface. We used a circular array of geophones on the trench wall to directly measure the degree of seismic anisotropy in saprolite and employed constant head infiltration tests to quantify hydrologic conductivity anisotropy. In the following subsections we detail the data collection methodologies and subsequent results for these in situ measurements.

4.7 | In situ measurements of seismic anisotropy

To measure the seismic anisotropy of saprolite in situ, we instrumented the wall of the soil excavation with a circular array of geophones (Figure S1). The array had a radius of 0.35 m and its centre was roughly 1.75 m below the ground surface. To record particle motion perpendicular to a vertical wall, horizontal (transverse component) geophones were placed on spikes and pushed into the wall. The seismic source was located at the centre of the circle, for which we used a ball peen hammer. First arrival travel times were then picked from stacked data associated with multiple hammer swings (Figure S2).

To quantify per cent anisotropy, we converted first arrival travel times to velocities, which we then fit to a periodic function of the following form.

$$Vp(\theta) = \alpha * \cos(2\theta + \phi) + \overline{Vp} \quad (2)$$

In equation 2, Vp is the p-wave velocity, θ is the propagation direction, α is the amplitude of the fitted cosine function, ϕ is a phase shift corresponding to the dip of the rock fabric and $\overline{Vp}$ is the average wave speed of the fitted function. In this case, per cent anisotropy is equal to $100\% * 2\alpha/\overline{Vp}$. We computed values and uncertainties for all three of the fitting parameters, α, $\overline{Vp}$ and ϕ, using an iterative bootstrapping technique (Eppinger et al., 2021; Novitsky et al., 2018) by randomly removing one-quarter of the data and fitting the remaining three-fourths 500 times (Figure 8).

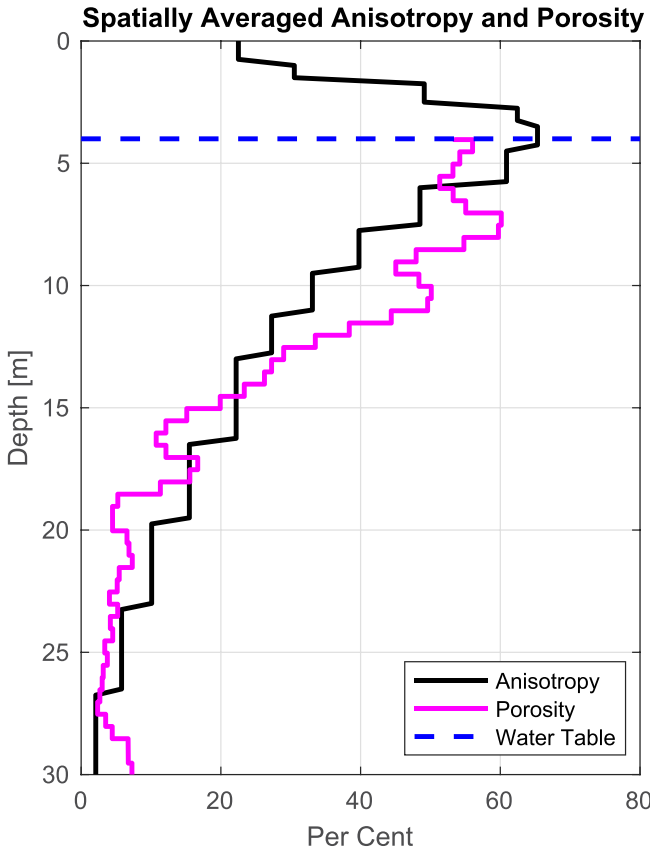

FIGURE 6 A plot comparing average seismic anisotropy measurements and porosity. By "average seismic anisotropy" we mean taking the average of all the one-dimensional anisotropy profiles created at each data window. The porosity log was measured using NMR at the borehole shown in Figure 1. Note that the seismic anisotropy profile and porosity log are not collocated but are within 3 km of each other. The depth of the water table measured in the borehole when the NMR data was collected is also shown.

4.8 | In situ measurements of conductivity anisotropy

To quantify saturated hydrologic conductivity anisotropy, we performed constant-head infiltration tests on in situ saprolite. These tests used a constant head permeameter (also known as an Amoozemeter) to allow water to flow under a steady hydraulic gradient into a predefined cylindrical volume surrounded by the media of interest. After the adjacent material becomes saturated, the hydrological conductivity can be measured by periodically recording the cumulative volume of water transmitted. To specifically sample saprolite, we dug two benches into the walls of the soil excavation such that the seats of the benches were saprolite planes (Figure 7). As noted in Figure 1C, we refer to these benches as sites A and B. At each bench, we then measured vertical conductivity by using a constant head permeameter to fill an open cylinder placed on the exposed foliation plane so that water would pool on the saprolite plane and flow downwards (Figure 7A). Next, to measure horizontal conductivity, we dug a relatively deep and narrow cylinder into the foliation planes comprising the seat of the bench. Since the surface area of the walls of this cylinder were significantly greater than the surface area of the bottom, flow in this cylinder was primarily lateral when we filled it with water (Figure 7B). However, a small amount of vertical flow in the latter infiltration test means that we slightly overestimate horizontal conductivity. Nonetheless, measuring mechanical and hydrological conductivity allows for an analogous conductivity per cent anisotropy measurement equal to $100^*2(K_h - K_v)/(K_h + K_v)$.

4.9 | In situ measurement results

The seismic survey results sampling saprolite 1.75 m below the ground surface on the wall of the excavation show seismic anisotropy measurements of 70.1 ± 3.5% (Figure 8). This agrees with the range of seismic anisotropy values constrained by the surface wave method (Figures 5 and 6). The seismic experiment also shows that the fast direction of wave propagation is roughly horizontal (Figure 8), aligning with the orientation of foliation planes observed in the excavation (Figures 2C and S1). Moreover, hydrologic conductivity is higher along foliation planes (horizontally) than across foliation planes (vertically) (Table 1), indicating good qualitative agreement between seismic and hydrologic anisotropy. The variance in the hydrologic conductivity measurements between the two sites (A and B) is consistent with previously observed spatial variations in soil permeability (Mirus, 2015).

5 | DISCUSSION

5.1 | A conceptual model of coupled anisotropy and porosity development via in situ weathering

Our data show that seismic anisotropy and porosity may correlate strongly in landscapes underlain by foliated bedrock (Figure 6). Why might this be so? Since porosity development in the CZ is driven by weathering, our results imply that CZ porosity develops alongside seismic anisotropy in foliated rocks. Here we consider the physical, chemical and biological sources of weathering, and how those processes might interact with rock fabric, and thereby also enhance seismic anisotropy.

Physical weathering comprises fracturing processes, including subcritical cracking and the opening of pre-existing fractures. The substantial role of subcritical cracking in generating new fractures and extending existing ones is well established (Eppes & Keanini, 2017). Furthermore, in foliated rocks, fracture propagation via subcritical cracking will be primarily oriented parallel to foliation (Nara & Kaneko, 2006). Subcritical cracking should thus be particularly prevalent in saprolite, where reactive water (both liquid and vapour forms) comes into contact with the retained initial fabric (Eppes & Keanini, 2017). Seismic anisotropy may be further enhanced in saprolite through the opening of existing fractures due to topographic and tectonic stresses (Molnar, 2004; Moon et al., 2017; Slim et al., 2015; St. Clair et al., 2015). As rocks are more likely to fail along existing fabrics, rocks that experienced regional metamorphism may have more pre-existing fractures parallel or subparallel to their foliation. We also expect the reopening of existing fractures to be enhanced in saprolite, where the least compressive stress is low (Moon et al., 2017; St. Clair et al., 2015).

Chemical weathering processes may also serve to enhance seismic anisotropy in weathering metamorphic rocks. In particular, some mineral weathering reactions produce an increase in grain volume that

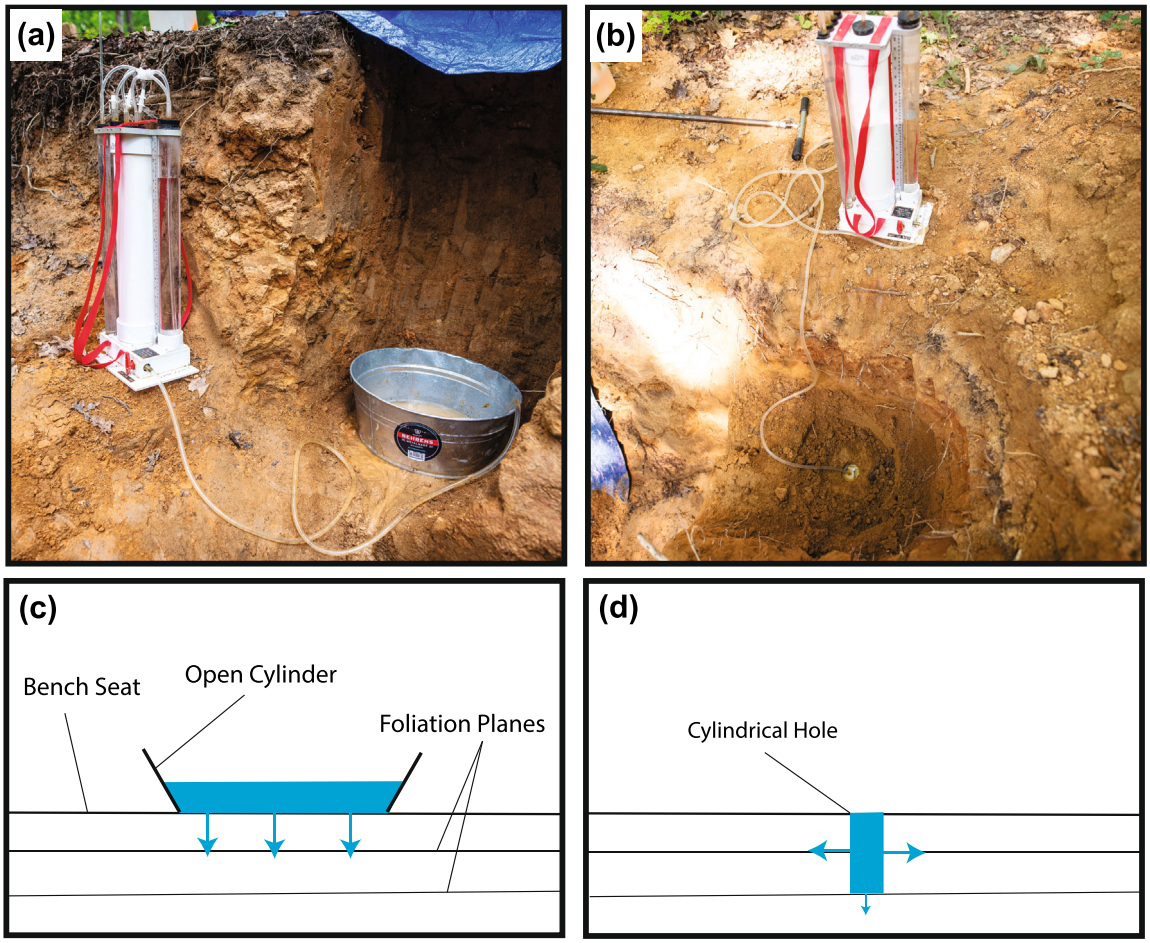

FIGURE 7 Panels A and B show snapshots of the vertical and horizontal conductivity tests, respectively. Panels C and D show simplified schematics of the same tests. Blue arrows in these schematics signify the flow of water.

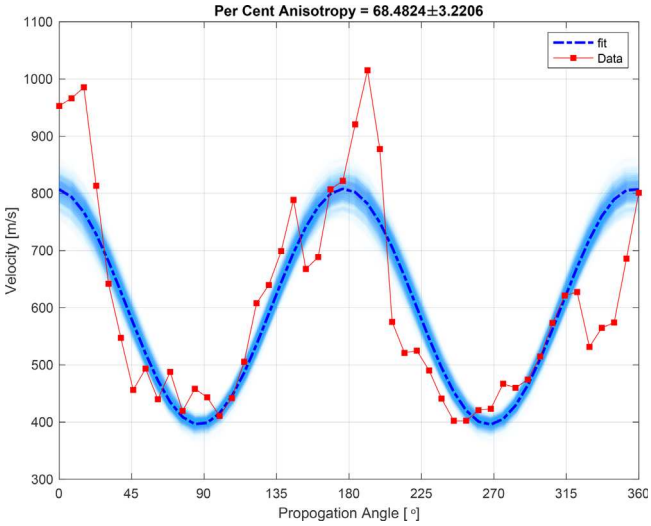

FIGURE 8 A summary of the results from measuring seismic anisotropy in situ on the wall of the excavation. Red squares show the measured velocity at each geophone as a function of propagation angle. On the x-axis, 0° means propagating horizontally to the left (when facing the excavation wall), 90° means propagating upwards, 180° signifies propagating to the right and 270° means downwardly propagating. Also plotted are transparent blue lines showing the fits for each of the 500 bootstrapping iterations. The dashed blue line is the fit using the mean parameters. Note that using the bootstrapping technique, we constrained the phase shift, ϕ, to be equal 0.693° ± 0.357°, which relates to the dip of the rock fabric was.

strains the weathered matrix. For example, clay-forming hydration reactions cause biotite grains to expand perpendicular to cleavage, thus promoting microcracking and wedging foliation planes apart (Buss et al., 2008; Fordham, 1990; Shen et al., 2019 ; Xu et al., 2022). The preferential removal of material could also lead to enhanced seismic anisotropy during the weathering of foliated rock. Chemical weathering will preferentially attack layers with less quartz and more weatherable minerals such as biotite and feldspar (Brantley, Lebedeva, et al., 2017; Fordham, 1990), leaving behind saprolite resembling a quartz skeleton with interspersed clay minerals and pore space.

These processes can be enhanced by biological weathering in the shallow CZ. The aperture of existing fractures and foliation could be increased by the growth of roots as plants exploit existing rock fabric to access the subsurface (Brantley, Eissenstat, et al., 2017; Pawlik et al., 2023). Not only may plants enhance existing fabric via root wedging, but through biogeochemical processes as well. Evidence of these biogeochemical processes at SCP include redoximorphic microsites which bear a distinctive horizontal striping pattern (Richter et al., 2014). This may signify enhanced biogeochemical weathering where roots have grown in between remnant foliation planes.

Whether through physical weathering such as the reopening of existing fractures due to topographic and tectonic stresses, chemical weathering in the manner of micro-cracking due to biotite expansion, chemophysical weathering like subcritical cracking, or biological weathering in the form of root wedging, in situ weathering processes

TABLE 1 Saturated hydrologic conductivity measurements of saprolite made in the soil excavation using the constant head permeator method.

Site	Vertical conductivity (mm/d)	Horizontal conductivity (mm/d)	Per cent anisotropy
A	6.1	30.2	132.8
B	3.3	7.0	71.8

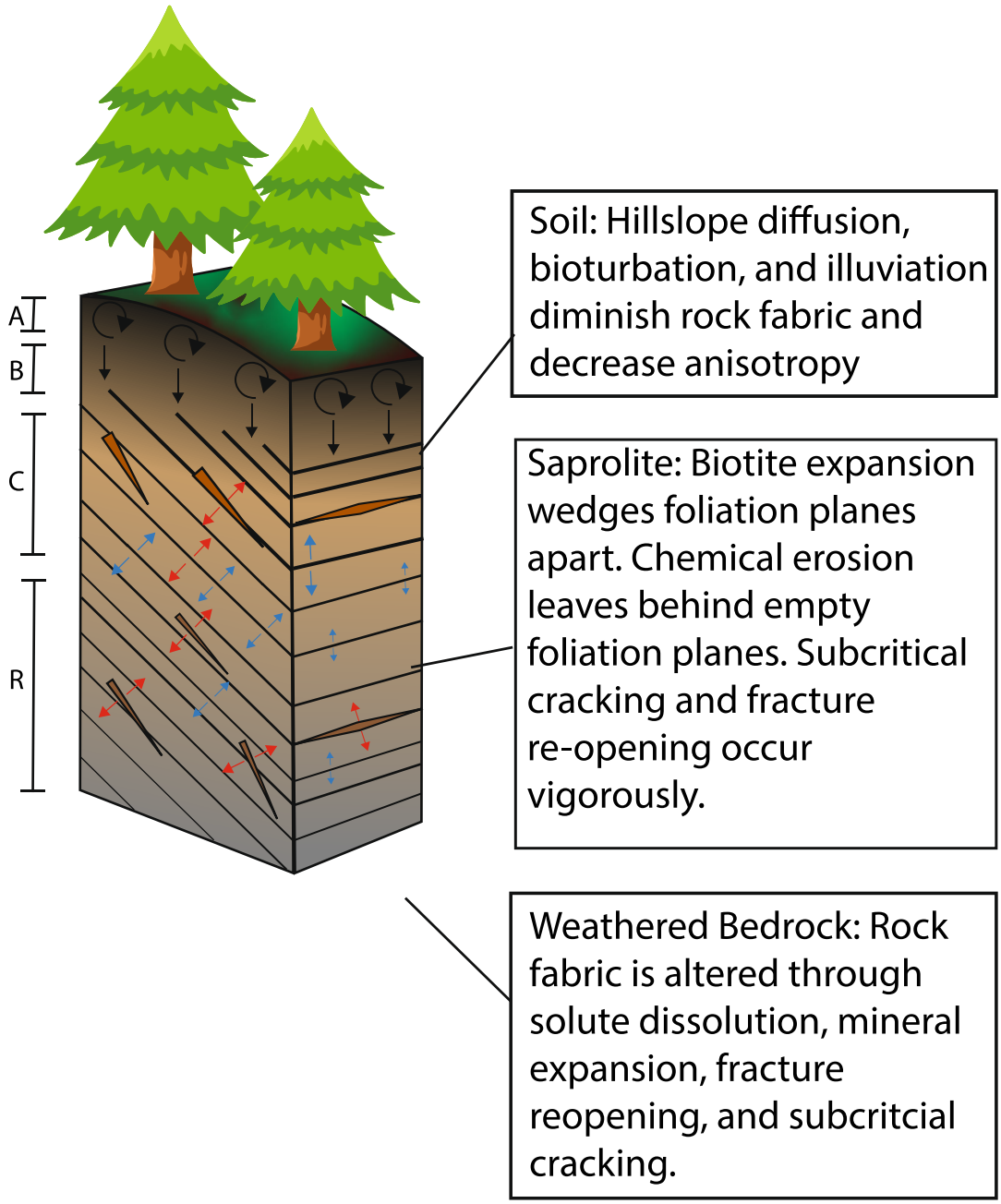

FIGURE 9 Conceptual model of anisotropy generation in the critical zone. Blue and red arrows signify chemical and physical processes, respectively. The depth ranges of soil horizons a, B, C and R are labelled.

can generate porosity and seismic anisotropy concurrently in the critical zone. This implies that porosity in the CZ may be structured as a direct consequence of geologic fabric in the weathering protolith. Our data also show that seismic anisotropy decreases upward in the shallowest subsurface, which is probably due to processes such as soil creep, pedoturbation and pedogenesis (Buol et al., 2011). Seismic anisotropy could also be decreased due to cracks, fractures and foliation being filled with downward percolating clay particles via illuviation (Buol et al., 2011).

Figure 9 provides a visual summary of how chemical and physical weathering processes create seismic anisotropy and interact with rock fabric in an idealized soil profile. In the weathered bedrock (R horizon), processes such as solute dissolution and fracture re-opening create localized weathering zones in rock fabric (Holbrook

et al., 2019). In saprolite (C horizon), in situ chemical and physical weathering processes accelerate, as chemical weathering replaces biotite and feldspar with clays (Brantley, Lebedeva, et al., 2017; Harman & Cosans, 2019), and fractures open due to microfracturing (Shen et al., 2019; Xu et al., 2022), subcritical cracking (Eppes & Keanini, 2017) and changes in topographic-tectonic stresses (Moon et al., 2017; St. Clair et al., 2015). In the B horizon, seismic anisotropy begins to diminish due to illuviation of clays into existing pore spaces (Buol et al., 2011). Finally, towards the ground surface in the A horizon, seismic anisotropy is destroyed by mixing processes such as soil creep and pedoturbation (Buol et al., 2011).

Ultimately, seismic anisotropy does not directly influence hillslope processes or landscape hydrology; however, because seismic anisotropy is indicative of mechanical and hydrological anisotropy, understanding how weathering processes affect seismic anisotropy can help inform how weathering affects other kinds as well. For example, foliation exerts a major control on a material's strength anisotropy (e.g., Acosta & Violay, 2020). Therefore, if rock fabric is affected by weathering in such a way that seismic anisotropy is enhanced, we expect that mechanical anisotropy would also increase due to the cohesive strength between fabric planes decreasing. Better understanding seismic anisotropy in the CZ could thus have implications for understanding erodibility and mass-wasting across landscapes. Seismic anisotropy can also be linked to the hydrological function of landscapes, as our infiltration tests show that saprolite exhibits hydrologic conductivity anisotropy aligning with rock fabric. These data imply that knowledge of the weathering protolith's geologic fabric (which is detectable through seismic anisotropy surveys) can help explain the flow and movement of water throughout catchments.

5.2 | Surface wave anisotropy imaging interpretation and outlook on future work

Using surface waves, we measure seismic anisotropy in the CZ with uniquely high resolution. Moreover, by using ensemble methods, we quantify uncertainty, which helps us know what interpretations we can make with confidence. For example, panels c and d of Figure 4 imply that velocity (and subsequently anisotropy) measurements in the upper ~15 m are well constrained. At depths greater than 15 m, the velocities are more uncertain (Figure 4), and consequently the deep anisotropy field is less well constrained. Nonetheless, it still seems likely that the anisotropy in the deep critical zone (15–30 m depth) is probably significantly lower than the anisotropy in the shallower subsurface. Specifically, it appears that high anisotropy values tend to occur in saprolite (Figure 5) where Flinchum et al. (2024) imaged material with negative Poisson's ratios. Negative Poisson's ratios have also been observed in saprolite by Trichandi et al. (2022). The connection between anisotropy and negative Poisson's ratios is still unclear, but there is some evidence that both may be related to crack formation in saprolite (Flinchum et al., 2024).

Observable seismic anisotropy is strongly dependent on the orientation of foliation, with tilted rock fabric showing less radial anisotropy than horizontal fabric (Okaya et al., 2019). Our interpretations apply to locations with horizontal fabric, which may not exist everywhere in our study site. However, we note that nearly horizontal rock fabric is observed in the soil excavation (Figure 2) and in the borehole located less than 3 km away from the seismic line (Holbrook et al., 2019). Nevertheless, slight changes in rock fabric orientation might produce variations in observable radial anisotropy. This could explain some of the apparent lateral variations in radial anisotropy seen in Figure 5. Future work could leverage this by using variations in apparent radial anisotropy to detect changes in the orientation of rock fabric. 3D multicomponent data collection, for example, would allow simultaneous observation of both shear wave splitting and directional variations in propagation velocity (Okaya et al., 2019). This could lead to delineating the orientation and prevalence of rock fabric in three dimensions across landscapes. A future geophysical study of this kind could have many potential applications, including helping pedologists to map fabric in soils, geomorphologists to better predict slope failure and hydrologists to estimate conductivity anisotropy across landscapes.

Future work may also seek to better understand the relationship between porosity and seismic anisotropy in landscapes underlain by other rock types. Past studies on seismic anisotropy in the CZ have been situated in areas with fractured granite (Novitsky et al., 2018) or garnet-bearing schist bedrock (Eppinger et al., 2021). Future studies may wish to build on previous work studying weathering in sedimentary rocks (e.g., Hudson Rasmussen et al., 2023; West et al., 2019) by investigating the relationship between seismic anisotropy and porosity in these areas. We expect the empirical relationship between seismic anisotropy and porosity (e.g., Figure S3) to vary with different rock types, although exactly how remains a promising direction for future research. Our novel method for constraining seismic anisotropy in the CZ using surface waves can be applied in new areas as to help further elucidate connections between weathering, rock fabric and landscape processes.

6 | CONCLUSIONS

We present the first case study using surface waves to measure radial anisotropy in the critical zone. This method is advantageous because it has the unique capacity to detect rock fabric with high resolution across landscapes. We find a remarkable correlation between seismic anisotropy measurements and NMR-derived porosity data. We explain this correlation by developing a conceptual framework that encompasses how weathering processes cause anisotropy and porosity to develop concurrently. Significant seismic anisotropy measured in situ suggests notable mechanical/strength anisotropy in saprolite. This leads to natural questions about how anisotropy affects slope stability and other geomorphological dynamics. In situ testing of hydrological conductivity anisotropy in saprolite demonstrates that rock fabric enhanced by weathering and inherited in saprolite may have a strong influence on the flow of groundwater. These findings show that rock fabric can play an important role in determining critical zone structure, function and properties.

ACKNOWLEDGEMENTS

This study was supported by the National Science Foundation award "Collaborative Research: Network Cluster: Bedrock controls on the deep critical zone, landscapes, and ecosystems" NSF-EAR 2012353 (Holbrook), 2012227 (Flinchum), 2012357 (Riebe, Grana, and Carr), 2012316 (Hayes), 2012264 (Harman) and an NSF Graduate Research Fellowship awarded to Eppinger.

AUTHOR CONTRIBUTIONS

Benjamin J Eppinger: conceptualization, funding acquisition, methodology, investigation, software, writing – initial draft, writing – reviewing and editing. **W. Steven Holbrook:** conceptualization, funding acquisition, supervision, writing – initial draft, writing – reviewing and editing. **Brady A. Flinchum:** investigation, resources, writing – reviewing and editing, supervision. **Dario Grana:** funding acquisition, methodology, software, supervision, writing – reviewing and editing. **Daniel de B. Richter:** resources, writing – reviewing and editing. **Jorden L. Hayes:** conceptualization, writing – reviewing and editing. **Clifford S. Riebe:** funding acquisition, writing – reviewing and editing. **Ciaran J. Harman:** investigation, resources. **Bradley J. Carr:** investigation, resources.

DATA AVAILABILITY STATEMENT

Upon acceptance of this manuscript, the authors will upload all geophysical data and derived products to the CUAHSI-managed on-line database HydroShare.

The data that support the findings of this study are available in the BCZN South Carolina Piedmont Data Repository at https://www.hydroshare.org/resource/d0d9c63a7a794129a247b2cfd617ad13/.

ORCID

Benjamin J. Eppinger https://orcid.org/0000-0002-1920-4519
W. Steven Holbrook https://orcid.org/0000-0003-0065-8841
Brady A. Flinchum https://orcid.org/0000-0003-0395-0450
Dario Grana https://orcid.org/0000-0003-4220-053X
Jorden L. Hayes https://orcid.org/0000-0001-5967-3953
Clifford S. Riebe https://orcid.org/0000-0002-8744-8208
Ciaran J. Harman https://orcid.org/0000-0002-3185-002X
Bradley J. Carr https://orcid.org/0000-0002-1378-4911

REFERENCES

Acosta, M. & Violay, M. (2020) Mechanical and hydraulic transport properties of transverse-isotropic gneiss deformed under deep reservoir stress and pressure conditions. *International Journal of Rock Mechanics and Mining Sciences*, 130, 104235. Available from: https://doi.org/10.1016/j.ijrmms.2020.104235

Befus, K.M., Sheehan, A.F., Leopold, M., Anderson, S.P. & Anderson, R.S. (2011) Seismic constraints on critical zone architecture, Boulder Creek watershed, front range, Colorado. *Vadose Zone Journal*, 10(3), 915–927. Available from: https://doi.org/10.2136/vzj2010.0108

Bergamo, P., Boiero, D. & Socco, L.V. (2012) Retrieving 2D structures from surface-wave data by means of space-varying spatial windowing. *Geophysics*, 77(4), EN39–EN51. Available from: https://doi.org/10.1190/geo2012-0031.1

Binley, A., Hubbard, S.S., Huisman, J.A., Revil, A., Robinson, D.A., Singha, K., et al. (2015) The emergence of hydrogeophysics for improved understanding of subsurface processes over multiple scales. *Water Resources Research*, 51(6), 3837–3866. Available from: https://doi.org/10.1002/2015WR017016

Bonetti, S., Richter, D.D. & Porporato, A. (2019) The effect of accelerated soil erosion on hillslope morphology. *Earth Surface Processes and Landforms*, 44(15), 3007–3019. Available from: https://doi.org/10.1002/esp.4694

Brantley, S.L., Eissenstat, D.M., Marshall, J.A., Godsey, S.E., Balogh-Brunstad, Z., Karwan, D.L., et al. (2017) Reviews and syntheses: on the roles trees play in building and plumbing the critical zone. *Biogeosciences*, 14(22), 5115–5142. Available from: https://doi.org/10.5194/bg-14-5115-2017

Brantley, S.L., Goldhaber, M.B. & Ragnarsdottir, K.V. (2007) Crossing disciplines and scales to understand the critical zone. *Elements*, 3(5), 307–314. Available from: https://doi.org/10.2113/gselements.3.5.307

Brantley, S.L., Lebedeva, M.I., Balashov, V.N., Singha, K., Sullivan, P.L. & Stinchcomb, G. (2017) Toward a conceptual model relating chemical reaction fronts to water flow paths in hills. *Geomorphology*, 277, 100–117. Available from: https://doi.org/10.1016/j.geomorph.2016.09.027

Buol, S.W., Southard, R.J., Graham, R.C. & McDaniel, P.A. (2011) *Soil genesis and classification*, 5th edition. Blackwell Pub. Available from: https://doi.org/10.1002/9780470960622.ch1

Buss, H.L., Sak, P.B., Webb, S.M. & Brantley, S.L. (2008) Weathering of the Rio Blanco quartz diorite, Luquillo Mountains, Puerto Rico: coupling oxidation, dissolution, and fracturing. *Geochimica et Cosmochimica Acta*, 72(18), 4488–4507. Available from: https://doi.org/10.1016/j.gca.2008.06.020

Callahan, R.P., Riebe, C.S., Pasquet, S., Ferrier, K.L., Grana, D., Sklar, L.S., et al. (2020) Subsurface weathering revealed in hillslope-integrated porosity distributions. *Geophysical Research Letters*, 47(15), e2020GL088322. Available from: https://doi.org/10.1029/2020GL088322

Callahan, R.P., Riebe, C.S., Sklar, L.S., Pasquet, S., Ferrier, K.L., Hahm, W.J., et al. (2022) Forest vulnerability to drought controlled by bedrock composition. *Nature Geoscience*, 15(9), 714–719. Available from: https://doi.org/10.1038/s41561-022-01012-2

Clavaud, J., Maineult, A., Zamora, M., Rasolofosaon, P. & Schlitter, C. (2008) Permeability anisotropy and its relations with porous medium structure. *Journal of Geophysical Research: Solid Earth*, 113(B1), 2007JB005004. Available from: https://doi.org/10.1029/2007JB005004

Duret, F., Shapiro, N.M., Cao, Z., Levin, V., Molnar, P. & Roecker, S. (2010) Surface wave dispersion across Tibet: direct evidence for radial anisotropy in the crust. *Geophysical Research Letters*, 37(16), 2010GL043811. Available from: https://doi.org/10.1029/2010GL043811

Emerick, A.A. & Reynolds, A.C. (2013) Ensemble smoother with multiple data assimilation. *Computers & Geosciences*, 55, 3–15. Available from: https://doi.org/10.1016/j.cageo.2012.03.011

Endrun, B., Meier, T., Lebedev, S., Bohnhoff, M., Stavrakakis, G. & Harjes, H.-P. (2008) *S* velocity structure and radial anisotropy in the Aegean region from surface wave dispersion. *Geophysical Journal International*, 174(2), 593–616. Available from: https://doi.org/10.1111/j.1365-246X.2008.03802.x

Eppes, M. & Keanini, R. (2017) Mechanical weathering and rock erosion by climate-dependent subcritical cracking. *Reviews of Geophysics*, 55(2), 470–508. Available from: https://doi.org/10.1002/2017RG000557

Eppinger, B.J., Hayes, J.L., Carr, B.J., Moon, S., Cosans, C.L., Holbrook, W.S., et al. (2021) Quantifying depth-dependent seismic anisotropy in the critical zone enhanced by weathering of a Piedmont schist. *Journal of Geophysical Research: Earth Surface*, 126(10), e2021JF006289. Available from: https://doi.org/10.1029/2021JF006289

Evensen, G. 2009. *Data assimilation: the ensemble Kalman filter*. Springer Berlin Heidelberg. https://doi.org/10.1007/978-3-642-03711-5

Fichtner, A., Kennett, B.L.N., Tsai, V.C., Thurber, C.H., Rodgers, A.J., Tape, C., et al. (2024) Seismic tomography 2024. *Bulletin of the Seismological Society of America*, 114(3), 1185–1213. Available from: https://doi.org/10.1785/0120230229

Flinchum, B.A., Grana, D., Carr, B.J., Ravichandran, N., Eppinger, B. & Holbrook, W.S. (2024) Low V_p/V_s values as an indicator for fractures in the critical zone. *Geophysical Research Letters*, 51(2), e2023GL105946. Available from: https://doi.org/10.1029/2023GL105946

Fordham, A.W. (1990) Weathering of biotite into dioctahedral clay minerals. *Clay Minerals*, 25(1), 51–63. Available from: https://doi.org/10.1180/claymin.1990.025.1.06

Friederich, W. & Huang, Z.-X. (1996) Evidence for upper mantle anisotropy beneath southern Germany from love and Rayleigh wave dispersion. *Geophysical Research Letters*, 23(10), 1135–1138. Available from: https://doi.org/10.1029/96GL01216

Gardner, G.H.F., Gardner, L.W. & Gregory, A.R. (1974) Formation velocity and density—the diagnostic basics for stratigraphic traps. *Geophysics*, 39(6), 770–780. Available from: https://doi.org/10.1190/1.1440465

Glastonbury, J. & Fell, R. (2010) Geotechnical characteristics of large rapid rock slides. *Canadian Geotechnical Journal*, 47(1), 116–132. Available from: https://doi.org/10.1139/T09-080

Harman, C.J. & Cosans, C.L. (2019) A low-dimensional model of bedrock weathering and lateral flow coevolution in hillslopes: 2. Controls on weathering and permeability profiles, drainage hydraulics, and solute export pathways. *Hydrological Processes*, 33(8), 1168–1190. Available from: https://doi.org/10.1002/hyp.13385

Haskell N. A. (1951) The dispersion of surface waves on multilayered media.

Hayes, J.L., Riebe, C.S., Holbrook, W.S., Flinchum, B.A. & Hartsough, P.C. (2019) Porosity production in weathered rock: where volumetric strain dominates over chemical mass loss. *Science Advances*, 5-(9), eaao0834. Available from: https://doi.org/10.1126/sciadv.aao0834

Herrmann, R.B. (2013) Computer programs in seismology: an evolving tool for instruction and research. *Seismological Research Letters*, 84(6), 1081–1088. Available from: https://doi.org/10.1785/0220110096

Herrmann, R. B., & Ammon, C. J. (2007) Surface waves, receiver functions and crustal structure. In: *Computer programs in seismology*, *Version 3.30*. Saint Louis University. Available from: http://www.eas.slu.edu/People/RBHerrmann/CPS330.html

Hertrich, M. (2008) Imaging of groundwater with nuclear magnetic resonance. *Progress in Nuclear Magnetic Resonance Spectroscopy*, 53(4), 227–248. Available from: https://doi.org/10.1016/j.pnmrs.2008.01.002

Holbrook, W.S., Marcon, V., Bacon, A.R., Brantley, S.L., Carr, B.J., Flinchum, B.A., et al. (2019) Links between physical and chemical weathering inferred from a 65-m-deep borehole through earth's critical zone. *Scientific Reports*, 9(1), 4495. Available from: https://doi.org/10.1038/s41598-019-40819-9

Holbrook, W.S., Riebe, C.S., Elwaseif, M., Hayes J, L., Basler-Reeder, K., Harry D, L., et al. (2014) Geophysical constraints on deep weathering and water storage potential in the southern sierra critical zone observatory. *Earth Surface Processes and Landforms*, 39(3), 366–380. Available from: https://doi.org/10.1002/esp.3502

Huang, H., Yao, H. & Van Der Hilst, R.D. (2010) Radial anisotropy in the crust of SE Tibet and SW China from ambient noise interferometry. *Geophysical Research Letters*, 37(21), 2010GL044981. Available from: https://doi.org/10.1029/2010GL044981

Hudson Rasmussen, B.M., Huang, M., Hahm, W.J., Rempe, D.M., Dralle, D. & Nelson, M.D. (2023) Mapping variations in bedrock weathering with slope aspect under a sedimentary ridge-valley system using near-surface geophysics and drilling. *Journal of Geophysical Research: Earth Surface*, 128(7), e2023JF007254. Available from: https://doi.org/10.1029/2023JF007254

Lebedeva, M.I. & Brantley, S.L. (2013) Exploring geochemical controls on weathering and erosion of convex hillslopes: beyond the empirical regolith production function. *Earth Surface Processes and Landforms*, 38(15), 1793–1807. Available from: https://doi.org/10.1002/esp.3424

Leone, J.D., Holbrook, W.S., Riebe, C.S., Chorover, J., Ferré, T.P.A., Carr, B.J., et al. (2020) Strong slope-aspect control of regolith thickness by bedrock foliation. *Earth Surface Processes and Landforms*, 45(12), 2998–3010. Available from: https://doi.org/10.1002/esp.4947

Ma, L., Oakley, D., Nyblade, A., Moon, S., Accardo, N., Wang, W., et al. (2021) Seismic imaging of a shale landscape under compression shows limited influence of topography-induced fracturing. *Geophysical Research Letters*, 48(17), e2021GL093372. Available from: https://doi.org/10.1029/2021GL093372

Mirus, B.B. (2015) Evaluating the importance of characterizing soil structure and horizons in parameterizing a hydrologic process model. *Hydrological Processes*, 29(21), 4611–4623. Available from: https://doi.org/10.1002/hyp.10592

Molnar, P. (2004) Interactions among topographically induced elastic stress, static fatigue, and valley incision. *Journal of Geophysical Research: Earth Surface*, 109(F2), 2003JF000097. Available from: https://doi.org/10.1029/2003JF000097

Montagner, J. & Nataf, H. (1986) A simple method for inverting the azimuthal anisotropy of surface waves. *Journal of Geophysical Research: Solid Earth*, 91(B1), 511–520. Available from: https://doi.org/10.1029/JB091iB01p00511

Moon, S., Perron, J.T., Martel, S.J., Holbrook, W.S. & St. Clair, J. (2017) A model of three-dimensional topographic stresses with implications for bedrock fractures, surface processes, and landscape evolution. *Journal of Geophysical Research: Earth Surface*, 122(4), 823–846. Available from: https://doi.org/10.1002/2016JF004155

Moravec, B.G., White, A.M., Root, R.A., Sanchez, A., Olshansky, Y., Paras, B.K., et al. (2020) Resolving deep critical zone architecture in complex volcanic terrain. *Journal of Geophysical Research: Earth Surface*, 125(1), e2019JF005189. Available from: https://doi.org/10.1029/2019JF005189

Nara, Y. & Kaneko, K. (2006) Sub-critical crack growth in anisotropic rock. *International Journal of Rock Mechanics and Mining Sciences*, 43(3), 437–453. Available from: https://doi.org/10.1016/j.ijrmms.2005.07.008

Navarre-Sitchler, A., Brantley, S.L. & Rother, G. (2015) How porosity increases during incipient weathering of crystalline silicate rocks. *Reviews in Mineralogy and Geochemistry*, 80(1), 331–354. Available from: https://doi.org/10.2138/rmg.2015.80.10

Novitsky, C.G., Holbrook, W.S., Carr, B.J., Pasquet, S., Okaya, D. & Flinchum, B.A. (2018) Mapping inherited fractures in the critical zone using seismic anisotropy from circular surveys. *Geophysical Research Letters*, 45(7), 3126–3135. Available from: https://doi.org/10.1002/2017GL075976

Okaya, D., Vel, S.S., Song, W.J. & Johnson, S.E. (2019) Modification of crustal seismic anisotropy by geological structures ("structural geometric anisotropy"). *Geosphere*, 15(1), 146–170. Available from: https://doi.org/10.1130/GES01655.1

Okaya, D.A. & Christensen, N.I. (2002) Anisotropic effects of non-axial seismic wave propagation in foliated crustal rocks. *Geophysical Research Letters*, 29(11), 1507. Available from: https://doi.org/10.1029/2001GL014285

Okaya, D.A. & McEvilly, T.V. (2003) Elastic wave propagation in anisotropic crustal material possessing arbitrary internal tilt. *Geophysical Journal International*, 153(2), 344–358. Available from: https://doi.org/10.1046/j.1365-246X.2003.01896.x

Park, C.B., Miller, R.D. & Xia, J. (1998) Imaging dispersion curves of surface waves on multi-channel record. *SEG Technical Program Expanded Abstracts*, 1998, 1377–1380. Available from: https://doi.org/10.1190/1.1820161

Parsekian, A.D., Singha, K., Minsley, B.J., Holbrook, W.S. & Slater, L. (2015) Multiscale geophysical imaging of the critical zone. *Reviews of Geophysics*, 53(1), 1–26. Available from: https://doi.org/10.1002/2014RG000465

Pasquet, S. & Bodet, L. (2017) Swip: an integrated workflow for surface-wave dispersion inversion and profiling. *Geophysics*, 82(6), WB47–WB61. Available from: https://doi.org/10.1190/geo2016-0625.1

Pawlik, Ł., Gruba, P., Gałązka, A., Marzec-Grządziel, A., Kupka, D., Szopa, K., et al. (2023) Weathering and soil production under trees growing on sandstones – the role of tree roots in soil formation. *Science of the Total Environment*, 902, 166002. Available from: https://doi.org/10.1016/j.scitotenv.2023.166002

Pedrazas, M.A., Hahm, W.J., Huang, M., Dralle, D., Nelson, M.D., Breunig, R.E., et al. (2021) The relationship between topography, bedrock weathering, and water storage across a sequence of ridges and valleys. *Journal of Geophysical Research: Earth Surface*, 126(4), e2020JF005848. Available from: https://doi.org/10.1029/2020JF005848

Pradhan, R.M., Singh, A., Ojha, A.K. & Biswal, T.K. (2022) Structural controls on bedrock weathering in crystalline basement terranes and its implications on groundwater resources. *Scientific Reports*, 12(1), 11815. Available from: https://doi.org/10.1038/s41598-022-15889-x

Raykova, R.B. & Nikolova, S.B. (2003) Anisotropy in the earth's crust and uppermost mantle in southeastern Europe obtained from Rayleigh

and love surface waves. *Journal of Applied Geophysics*, 54(3–4), 247–256. Available from: https://doi.org/10.1016/j.jappgeo.2002.11.001

Rich, C.I. (1956) Muscovite weathering in a soil developed in the Virginia Piedmont. *Clays and Clay Minerals*, 5(1), 203–212. Available from: https://doi.org/10.1346/CCMN.1956.0050117

Richter, D.D., Markewitz, D., Trumbore, S.E. & Wells, C.G. (1999) Rapid accumulation and turnover of soil carbon in a re-establishing forest. *Nature*, 400(6739), 56–58. Available from: https://doi.org/10.1038/21867

Richter, D.dB., Bacon, A.R., Billings, S.A., Binkley, D., Buford, M., Callaham, M.A., et al. (2014) Evolution of Soil, Ecosystem, and Critical Zone Research at the USDA FS Calhoun Experimental Forest. In: Hayes, D.C., Stout, S.L., Crawford, R.H. & Hoover, A.P. (Eds.) *USDA Forest Service experimental forests and ranges*. Springer New York, pp. 405–433 https://doi.org/10.1007/978-1-4614-1818-4_18

Riebe, C.S., Hahm, W.J. & Brantley, S.L. (2017) Controls on deep critical zone architecture: a historical review and four testable hypotheses. *Earth Surface Processes and Landforms*, 42(1), 128–156. Available from: https://doi.org/10.1002/esp.4052

Roth, R.A. (1983) Factors affecting landslide-susceptibility in San Mateo County, California. *Environmental & Engineering Geoscience*, xx(4), 353–372. Available from: https://doi.org/10.2113/gseegeosci.xx.4.353

Sak, P.B., Navarre-Sitchler, A.K., Miller, C.E., Daniel, C.C., Gaillardet, J., Buss, H.L., et al. (2010) Controls on rind thickness on basaltic andesite clasts weathering in Guadeloupe. *Chemical Geology*, 276(3–4), 129–143. Available from: https://doi.org/10.1016/j.chemgeo.2010.05.002

Seyfried, M., Lohse, K., Marks, D., Flerchinger, G., Pierson, F. & Holbrook, W.S. (2018) Reynolds Creek experimental watershed and critical zone observatory. *Vadose Zone Journal*, 17(1), 1–20. Available from: https://doi.org/10.2136/vzj2018.07.0129

Shen, X., Arson, C., Ferrier, K.L., West, N. & Dai, S. (2019) Mineral weathering and bedrock weakening: modeling microscale bedrock damage under biotite weathering. *Journal of Geophysical Research: Earth Surface*, 124(11), 2623–2646. Available from: https://doi.org/10.1029/2019JF005068

Singha, K., Sullivan, P.L., Billings, S.A., Walls, L., Li, L., Jarecke, K.M., et al. (2024) Expanding the spatial reach and human impacts of critical zone science. *Earth's Future*, 12(3), e2023EF003971. Available from: https://doi.org/10.1029/2023EF003971

Slim, M., Perron, J.T., Martel, S.J. & Singha, K. (2015) Topographic stress and rock fracture: a two-dimensional numerical model for arbitrary topography and preliminary comparison with borehole observations. *Earth Surface Processes and Landforms*, 40(4), 512–529. Available from: https://doi.org/10.1002/esp.3646

Socco, L.V., Foti, S. & Boiero, D. (2010) Surface-wave analysis for building near-surface velocity models—established approaches and new perspectives. *Geophysics*, 75(5), 75A83–75A102. Available from: https://doi.org/10.1190/1.3479491

Socco, L.V. & Strobbia, C. (2004) Surface-wave method for near-surface characterization: a tutorial. *Near Surface Geophysics*, 2(4), 165–185. Available from: https://doi.org/10.3997/1873-0604.2004015

St. Clair, J., Moon, S., Holbrook, W.S., Perron, J.T., Riebe, C.S., Martel, S.J., et al. (2015) Geophysical imaging reveals topographic stress control of bedrock weathering. *Science*, 350(6260), 534–538. Available from: https://doi.org/10.1126/science.aab2210

Trichandi, R., Bauer, K., Ryberg, T., Scherler, D., Bataille, K. & Krawczyk, C.M. (2022) Combined seismic and borehole investigation of the deep granite weathering structure—Santa Gracia reserve case in Chile. *Earth Surface Processes and Landforms*, 47(14), 3302–3316. Available from: https://doi.org/10.1002/esp.5457

Tromp, J. (2019) Seismic wavefield imaging of earth's interior across scales. *Nature Reviews Earth & Environment*, 1(1), 40–53. Available from: https://doi.org/10.1038/s43017-019-0003-8

Walsh, J.B. & Brace, W.F. (1964) A fracture criterion for brittle anisotropic rock. *Journal of Geophysical Research*, 69(16), 3449–3456. Available from: https://doi.org/10.1029/JZ069i016p03449

West, N., Kirby, E., Nyblade, A.A. & Brantley, S.L. (2019) Climate preconditions the critical zone: elucidating the role of subsurface fractures in the evolution of asymmetric topography. *Earth and Planetary Science Letters*, 513, 197–205. Available from: https://doi.org/10.1016/j.epsl.2019.01.039

Xia, J., Miller, R.D. & Park, C.B. (1999) Estimation of near-surface shear-wave velocity by inversion of Rayleigh waves. *Geophysics*, 64(3), 691–700. Available from: https://doi.org/10.1190/1.1444578

Xie, J., Ritzwoller, M.H., Shen, W., Yang, Y., Zheng, Y. & Zhou, L. (2013) Crustal radial anisotropy across eastern Tibet and the Western Yangtze craton. *Journal of Geophysical Research: Solid Earth*, 118(8), 4226–4252. Available from: https://doi.org/10.1002/jgrb.50296

Xu, T., Shen, X., Reed, M., West, N., Ferrier, K.L. & Arson, C. (2022) Anisotropy and microcrack propagation induced by weathering, regional stresses and topographic stresses. *Journal of Geophysical Research: Solid Earth*, 127(7), e2022JB024518. Available from: https://doi.org/10.1029/2022JB024518

Zaslavsky, D. & Rogowski, A.S. (1969) Hydrologic and morphologic implications of anisotropy and infiltration in soil profile development. *Soil Science Society of America Journal*, 33(4), 594–599. Available from: https://doi.org/10.2136/sssaj1969.03615995003300040031x

SUPPORTING INFORMATION

Additional supporting information can be found online in the Supporting Information section at the end of this article.

How to cite this article: Eppinger, B.J., Holbrook, W.S., Flinchum, B.A., Grana, D., Richter, D.B., Hayes, J.L. et al. (2025) On the role of inherited rock fabric in critical zone porosity development: Insights from seismic anisotropy measurements using surface waves. *Earth Surface Processes and Landforms*, 50(9), e70132. Available from: https://doi.org/10.1002/esp.70132